

# Investigation of the Structural and Dynamical Properties of the (001) Surface of $\text{LiCu}_2\text{O}_2$

Yangyang Yao<sup>1</sup>, Xuetao Zhu<sup>1</sup>, H. C. Hsu<sup>2</sup>, F. C. Chou<sup>2</sup> and M. El-Batanouny<sup>1</sup>

<sup>1</sup> Physics Department, Boston University, Boston, MA 02215

<sup>2</sup> Center of Condensed Matter Sciences, National Taiwan University, Taipei 10617, Taiwan

We report on studies of the structure and dynamics of the (001) surface of single crystal  $\text{LiCu}_2\text{O}_2$ , investigated by He beam scattering at room temperature, and with lattice dynamical models. The best fit surface corrugation to measured diffraction patterns shows that the surface termination is exclusively a  $\text{Li}^{+1}\text{Cu}^{+2}\text{O}^{-2}$  plane. Lattice dynamics fits to inelastic He scattering spectra reveal the presence of two low-lying surface phonon modes, identified with the motion of  $\text{Cu}^{+2}$ ,  $\text{Li}^{+1}$  surface ions normal to the surface.

## I. INTRODUCTION

$\text{LiCu}_2\text{O}_2$  continues to attract considerable attention because of the unique physical properties it exhibits. Initially, interest in this system was stimulated by the presence of double-chain ladders of  $\text{Cu}^{+2}\text{O}$ , which presented a prototype quasi-one-dimensional (QOD) spin-1/2 quantum magnetic system with competing magnetic interactions. Competing magnetic interactions in the double-chain ladder were known to give rise to geometric frustration, which in turn is manifest in an ordered incommensurate helimagnetic phase at low temperatures. It was expected that the presence of  $S=1/2$  spins would give rise to strongly competing commensurate quantum spin fluctuations that tend to suppress the transition temperature<sup>1,2,3</sup>. More recently, it was discovered that this system exhibits ferroelectricity upon the emergence of the spiral magnetic order. This renders  $\text{LiCu}_2\text{O}_2$  as the second cuprate to join the list of multiferroics<sup>4,5,6,7</sup>.

A series of successive magnetic phases have been reported at low temperatures<sup>1,8,9</sup>: Electron spin resonance (ESR) measurements revealed the presence of a dimerized spin-singlet state at  $T > 23\text{K}$ , with an energy gap of  $\Delta=72\text{K}$  between the spin-singlet ground state and the first spin-triplet excited state. Magnetic neutron scattering measurements confirmed the existence of a QOD spin-ordered helical phase in the temperature range  $9\text{K} < T < 23\text{K}$ <sup>2,8</sup>, and a collinear anti-ferromagnetic (AFM) phase was suggested to exist below  $9\text{K}$ <sup>9,10,11</sup>. The presence of the QOD magnetic ordering was attributed to the presence of impurities in the chains: The observation of the classical helical phase in  $\text{LiCu}_2\text{O}_2$  was ascribed to substitutional  $\text{Li}^+$  defects that tend to suppress effective long-range one-dimensionality<sup>1</sup>.

$\text{LiCu}_2\text{O}_2$  is a quasi-1D insulator. It has a layered charge-ordered orthorhombic crystal structure belonging to the  $Pnma$  space group; the primitive cell has lattice constants  $a=5.73\text{\AA}$ ,  $b=2.86\text{\AA}$ ,  $c=12.47\text{\AA}$  respectively<sup>12</sup>. It is a mixed-valent compound with copper ions in the  $\text{Cu}^{+2}$  and  $\text{Cu}^{+1}$  valance states. The magnetic  $\text{Cu}^{+2}$  ( $S=1/2$ ) ions are located at the center of edge-sharing  $\text{CuO}_4$  plaquettes which form infinite chains along the crystallographic  $b$ -axis. Coplanar chains are connected by chains of Li ions along the  $a$ -axis, and two such planes

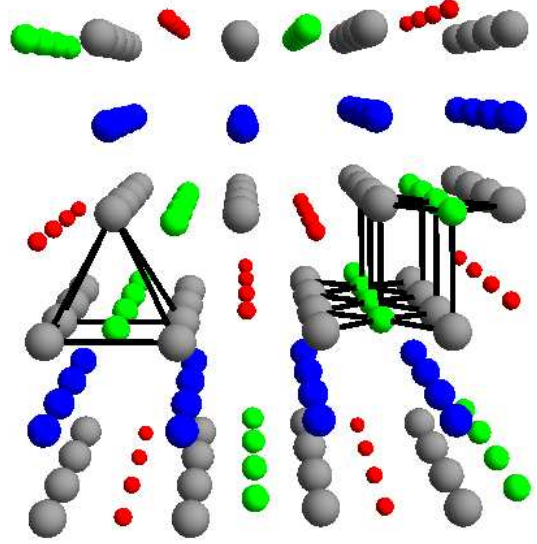


FIG. 1: Crystal structure of  $\text{LiCu}_2\text{O}_2$ . The color code is: Li (red), O (gray),  $\text{Cu}^{+1}$  (blue),  $\text{Cu}^{+2}$  (green)

form double-layers parallel to the  $ab$ -plane, as shown in figure 1. The QOD spin arrangement is due to these double chains of  $\text{Cu}^{+2}$  ions that run along the crystallographic  $b$  axis. The period of each leg of the double spin chains is equal to  $b$ . The two legs are offset by  $b/2$  relative to each other. Along the  $c$ -axis, each double-layer is separated from its double-layer neighbors by magnetically inert  $\text{Cu}^{+1}$  planes.

Despite the extensive studies of bulk structural and magnetic properties of  $\text{LiCu}_2\text{O}_2$  crystals cited above, no investigation of its surface properties has been reported in the literature. It is known that  $\text{LiCu}_2\text{O}_2$  crystals easily peel along the (001) surface. However, since these crystals consist of alternating double-layers of  $\text{Li}^{+1}\text{Cu}^{+2}\text{O}_2^{-2}$  and single layers of  $\text{Cu}^{+1}$ , it remains to be determined whether the cleavage would result in the coexistence of  $\text{Li}^{+1}\text{Cu}^{+2}\text{O}_2^{-2}$  and  $\text{Cu}^{+1}$  surfaces, or in an exclusive presence of one of these layer types. If the latter scenario occurs, then it would dictate that the double-layer must split in order to provide complete coverage of the two newly exposed surfaces. The double-layer splitting means

the splitting of the double-chain and the presence of a single-chain, which is expected to display different magnetic behavior from that observed in the double-chain.

In this paper we present the results of extensive studies of the (001) surface of  $\text{LiCu}_2\text{O}_2$ , using the experimental techniques of elastic and inelastic helium scattering aimed at determining its surface structural and dynamical properties, respectively. Furthermore, we used lattice dynamical models with slab geometries to interpret the surface phonon dispersion curves derived from the measured inelastic scattering spectra. The surface corrugation topography, derived from a large set of diffraction patterns, clearly shows that the surface termination is exclusively  $\text{Li}^{+1}\text{Cu}^{+2}\text{O}_2^{-2}$ . Moreover, empirical lattice dynamics models, with slab geometries based on such termination and fit to the inelastic experimental results, reveal two low-lying dispersion curves with polarizations normal to the surface, one involves the  $\text{Cu}^{+2}$  and the second involves Li ions. In section II the experimental setup and procedures are discussed, and the results and conclusion are presented in section III.

## II. EXPERIMENTAL SETUP AND PROCEDURE

Single crystals of  $\text{LiCu}_2\text{O}_2$  with high Li content of  $\approx 0.99 \pm 0.03$  were grown by the floating-zone method. The Li content was determined accurately through combined iodometric titration and thermogravimetric methods. This ruled out the possibility of chemical disorder between Li and Cu ions. Details of the growth procedures and stoichiometry conformation are given in Ref. 13. Typical crystal samples used were about  $3\text{mm} \times 3\text{mm} \times 2\text{mm}$  in size, with its exposed surface parallel to the *ab*-plane. The crystals were attached to an OFHC copper sample-holder by conductive silver epoxy. A cleaving (peeling) post was attached to the top sample surface in the similar way. The prepared sample holder was mounted on a sample manipulator equipped with XYZ motions as well as polar and azimuthal rotations. The pressure in the Ultra-High Vacuum (UHV) chamber was maintained at  $10^{-10}$  torr throughout the experiment to ensure the cleanliness of the sample surface during measurement performance. In situ cleaving under UHV conditions was effected by knocking off the cleaving post. Immediately after cleaving, the quality of the long-range ordering on the surface was confirmed by the appearance of sharp diffraction LEED spots.

A supersonic mono-energetic collimated helium beam, with velocity resolution better than 1.4 %, was generated by a nozzle-skimmer assembly and 2mm diameter collimating slits. The average beam velocity was varied by attaching the nozzle reservoir to a closed-cycle helium refrigerator, and controlling the reservoir temperature with the aid of a digital temperature controller (Scientific Instruments Model 9700) and a diode sensor attached to the reservoir. As a result, the beam energy can be var-

ied in the range 65meV to 21meV by varying the nozzle temperature from 300K to 110K. Polar rotation of the sample was used to vary the incident angle  $\theta_i$  with respect to the surface normal, while the azimuthal rotation was employed to align the scattering plane along a high-symmetry surface crystallographic direction. The scattered He beam was collected by an angle-resolved detector mounted on a two-axis goniometer, which allows the scattered angle  $\theta_f$  to be varied independently from  $\theta_i$ <sup>14</sup>, and allows in- and out-of the scattering-plane measurements. The detector<sup>15</sup> is comprised of an electron gun and a multichannel plate (MCP) electron multiplier. The electron gun generates a well-collimated, monoenergetic electron beam crossing the He beam at right angles. The energy of the electron beam is tuned to excite the He atoms to their first excited metastable state ( $2^3\text{S He}^*$ ) upon impact. Deexcitation of a  $\text{He}^*$  atom at the surface of the MCP leads to the ejection of an electron which generates an electron cascade that is then collected by the anode of the multiplier. By electronically pulsing the electron gun, a gate function is created for time-of-flight (TOF) measurements in the inelastic HAS mode. The details of the detection scheme are given in Ref 14. All measurements were performed with the sample surface at room temperature.

By writing the He-atom wave vector as  $\mathbf{k} = (\mathbf{K}, k_z)$ , where  $\mathbf{K}$  is the component parallel to the surface, conservation of momentum and energy for in-the-scattering-plane geometry can be expressed as

$$\Delta\mathbf{K} = \mathbf{G} + \mathbf{Q} = k_f \sin \theta_f - k_i \sin \theta_i \quad (1)$$

$$\Delta E = \hbar\omega(\mathbf{Q}) = E_i \left[ \left( \frac{\sin \theta_i + \Delta K/k_i}{\sin \theta_f} \right)^2 - 1 \right] \quad (2)$$

where subscripts i and f denote incident and scattered beams, respectively, and  $\Delta\mathbf{K}$  is the momentum transfer parallel to the surface.  $\mathbf{G}$  is a surface reciprocal-lattice vector,  $\mathbf{Q}$  is the surface phonon wave vector, and  $\hbar\omega(\mathbf{Q})$  is the corresponding surface phonon energy.  $E_i = \hbar^2 k_i^2 / 2M$ , where  $M$  is the mass of a He atom. By eliminating  $k_f$  from the above equations, one obtains the so-called scan curve relations which are the locus of all the allowed  $\Delta\mathbf{K}$  and  $\Delta E$  as dictated by the conservation relations,

$$\Delta E = E_i \left[ \left( \frac{\sin \theta_i + \Delta K/k_i}{\sin \theta_f} \right)^2 - 1 \right]. \quad (3)$$

The intersections of these scan curves with the phonon dispersion curves define the kinematically allowed inelastic events for a fixed geometric arrangement. Thus, by systematically changing  $E_i$ ,  $\theta_i$ , and  $\theta_f$ , the entire dispersion curves can be constructed.

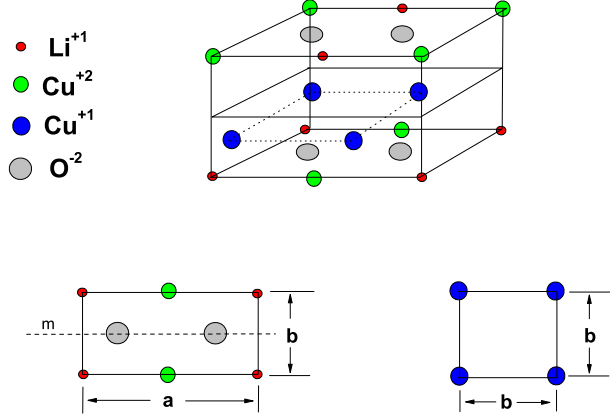


FIG. 2: Top: Half of a unit cell of  $\text{LiCu}_2\text{O}_2$ . Bottom: Two candidates for surface termination:  $\text{Cu}^{+1}$  layer with a square lattice (bottom right), or a  $\text{Li}^{+1}\text{Cu}^{+2}\text{O}_2^{-2}$  layer (bottom left).

### III. RESULTS AND DISCUSSION

#### A. Elastic He Scattering And Surface Structure

Diffraction patterns were collected from several crystal samples at a temperature of 300 K for several scattering conditions:

1. incident He wave numbers,  $k_i$ , in the range  $6.42\text{\AA}^{-1}$  and  $11.12\text{\AA}^{-1}$ ,
2. incident angles,  $\theta_i$ , between  $30^\circ$  and  $50^\circ$ , and
3. two high-symmetry azimuthal surface orientations,  $a$  and  $b$ , separated by  $90^\circ$ .

As was mentioned above, there are two candidates for the surface termination, which are shown in Figure 2, the  $\text{Li}^{+1}\text{Cu}^{+2}\text{O}_2^{-2}$  layer and the  $\text{Cu}^{+1}$  layer. The latter has a square lattice with lattice constant  $b$ , and  $C_{4v}$  symmetry. Thus, the diffraction peaks that correspond to odd multiples of  $2\pi/a$  should be absent for pure  $\text{Cu}^{+1}$  surface termination, which contradicts the fact that they do appear in all the measured diffraction patterns. Alternatively, for  $\text{Li}^{+1}\text{Cu}^{+2}\text{O}_2^{-2}$  termination, the well known crystal twinning<sup>1,6,7</sup> would imply that the two azimuthal orientations would give the same diffraction pattern. This means that we obtain a superposition of diffraction patterns from  $a\langle 10 \rangle$  and  $b\langle 01 \rangle$  directions. Moreover, since for  $\text{LiCu}_2\text{O}_2$   $a \simeq 2b$ , the diffraction peaks associated with the  $b$ -direction will lie very close to the even-order peaks obtained for the  $a$ -direction.

Figure 3 shows a typical diffraction pattern recorded for  $k_i = 7.28\text{\AA}^{-1}$  and  $\theta_i = 31.4^\circ$ . Although the twinning makes the situation a little complicated, luckily, the angular resolution in the diffraction pattern allows us to clearly separate the peak positions along the two directions, as indicated by peaks (2,0) and (0,1) in figure 3.

The coexistence of both surface terminations would imply that the intensity of the (1,0) and (0,1) peaks should be comparable, but, in fact, the (0,1) peak has exhibited appreciably lower intensity than the (1,0) peak. Hence, we shall follow the scenario of a purely  $\text{Li}^{+1}\text{Cu}^{+2}\text{O}_2^{-2}$  termination.

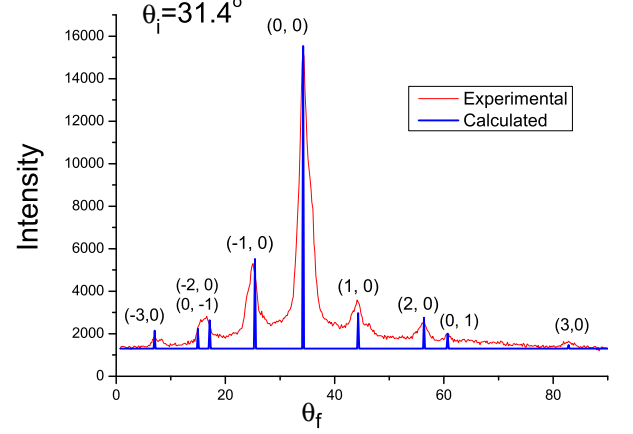


FIG. 3: The experimental diffraction pattern with  $k_i = 7.28\text{\AA}^{-1}$ ,  $\theta_i = 31.4^\circ$  at  $T=300\text{K}$  (red), and the calculated diffraction intensities (blue vertical bars)

The surface periodicity along  $a$  and  $b$  is derived from the positions of their corresponding diffraction peaks using the relation

$$|\mathbf{k}_i| (\sin \theta_i - \sin \theta_G) = |\mathbf{G}| \quad (4)$$

where  $\mathbf{k}_i$  is the incident beam wave-vector,  $\mathbf{G}$  a surface reciprocal lattice vector,  $\theta_G$  the corresponding scattering angle. Analysis of all the collected diffraction patterns yield the surface lattice constant values:  $a_s = 5.76 \pm 0.05\text{\AA}$  and  $b_s = 2.91 \pm 0.08\text{\AA}$ , which compares quite well with the bulk values of  $a=5.73\text{\AA}$ ,  $b=2.86\text{\AA}$  and, thus, precludes the presence of diffraction satellites and surface reconstruction.

In order to determine the topology of the surface primitive cell we used the *hard corrugated wall model* within the *eikonal approximation* to calculate the elastic scattering intensities<sup>16</sup>. Here, the surface topology is defined in terms of a surface corrugation function  $\zeta(\mathbf{R})$ <sup>17</sup>, where  $\mathbf{R}$  denotes a surface position vector and  $\zeta$  the corrugation height at that position. In this framework, the scattering amplitude of the diffraction peak  $\mathbf{G}$  is given by<sup>17</sup>

$$A_{\mathbf{G}} = -\frac{1}{S} \int_{\text{u.c.}} e^{i[\mathbf{G} \cdot \mathbf{R} + q_{\mathbf{G}z} \zeta(\mathbf{R})]} d\mathbf{R} \quad (5)$$

where  $q_{\mathbf{G}z} = k_{iz} - k_{Gz}$ , with  $k_{Gz} = k_i \cos \theta_G$ . The integration is carried over the unit cell (u.c.) of area  $S$ . Since  $\zeta(\mathbf{R})$  should have the surface periodicity, we write

$$\zeta(\mathbf{R}) = \sum_{\mathbf{G}} \zeta_{\mathbf{G}} \exp(i\mathbf{G} \cdot \mathbf{R}) \quad (6)$$

We make use of the reflection symmetry perpendicular to the  $b$ -direction ( $y$ -axis) of the  $\text{LiCu}_2\text{O}_2$  surface to simplify equation (6), and write

$$\zeta(x, y) = \sum_{n_1, n_2} \zeta_{n_1, n_2} \sin(n_1 b_1 x) \cos(n_2 b_2 y) + \sum_{n_3, n_4} \zeta_{n_3, n_4} \cos(n_3 b_1 x) \cos(n_4 b_2 y) \quad (7)$$

where  $b_1 = \frac{2\pi}{a}$ ,  $b_2 = \frac{2\pi}{b}$ , are the surface reciprocal lattice vector basis.

The goal now is to determine the coefficients  $\zeta_{\mathbf{G}}$ . The following iterative fitting scheme was adopted<sup>18</sup>. Initially, the magnitudes  $|A_{\mathbf{G}}|$  are determined from the experimental diffraction pattern using the geometric relation

$$P_{\mathbf{G}} = \frac{|k_{\mathbf{G}z}|}{|k_{iz}|} |A_{\mathbf{G}}|^2 \quad (8)$$

The experimental intensities are normalized to satisfy the unitarity condition

$$\sum_{\mathbf{G}} P_{\mathbf{G}} = 1 \quad (9)$$

Next, the eikonal equation<sup>16,17,18</sup>

$$\sum_{\mathbf{G}} A_{\mathbf{G}} e^{i\mathbf{G} \cdot \mathbf{R}} e^{ik_{\mathbf{G}z}} \zeta(\mathbf{R}) = -e^{ik_{iz}} \zeta(\mathbf{R}) \quad (10)$$

where  $A_{\mathbf{G}} = |A_{\mathbf{G}}| e^{i\phi_{\mathbf{G}}}$ , is used to determine  $\zeta(\mathbf{R})$ .  $\phi_{\mathbf{G}}$  is a diffraction phase angle to be determined. In the first iteration we set  $A_{\mathbf{G}} = |A_{\mathbf{G}}|$ , which yields

$$\zeta_0(\mathbf{R}) = \frac{\ln(-\sum_{\mathbf{G}} A_{\mathbf{G}} e^{i\mathbf{G} \cdot \mathbf{R}})}{2ik_{iz}},$$

where we replaced  $k_{\mathbf{G}z}$  by  $-k_{iz}$  in equation (10). Further iterations involved varying the amplitudes  $\zeta_{\mathbf{G}}$  around the values obtained from  $\zeta_0(\mathbf{R})$ .

After each iteration the reliability factor  $R$

$$R = \frac{1}{N} \sqrt{\sum_{\mathbf{G}} (P_{\mathbf{G}}^{\text{exp}} - P_{\mathbf{G}}^{\text{calc}})^2} \quad (11)$$

where  $N$  is the number of diffraction peaks, was calculated. The iterations were terminated when an acceptable small value of  $R$  was reached. The corrugation function with best-fit parameters,  $R = 0.003$ , is

$$\zeta(x, y) = -0.06 \cos(b_1 x) - 0.05 \cos(2b_1 x) + 0.02 \cos(3b_1 x) + 0.03 \sin(b_1 x) - 0.03 \cos(b_2 y) + 0.05 \cos(2b_2 y) - 0.07 \cos(b_2 y) \sin(2b_1 x) \quad (12)$$

It is plotted in figure 4, and the corresponding calculated diffraction peak intensities are shown as blue vertical bars in figure 3. The locations of the Li,  $\text{Cu}^{+2}$ , and the two O ions have been identified by comparing the positions of the corrugation maxima to ionic positions in the unit cell; they are indicated in the figure.

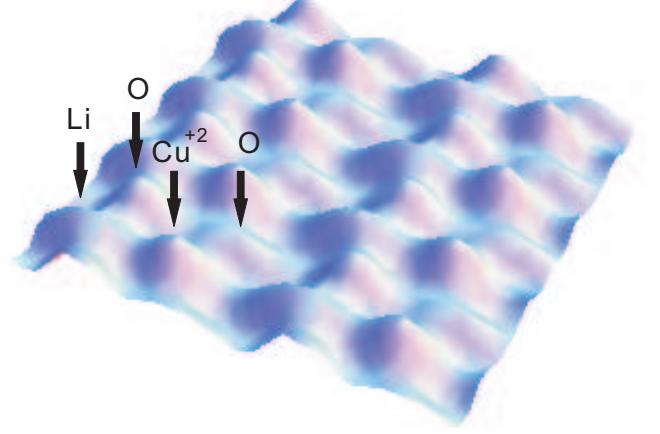


FIG. 4: Calculated surface corrugation function

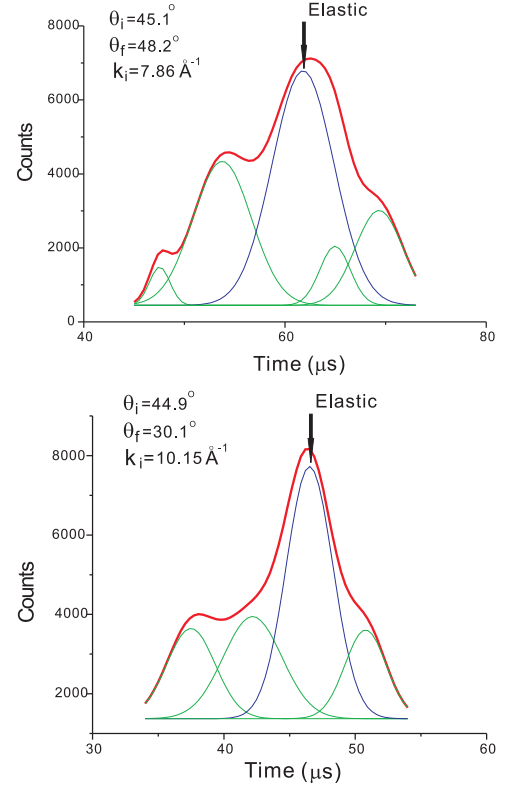


FIG. 5: Typical time-of-flight spectra. The experimental curve (red) is resolved into inelastic peaks (green) and the diffuse elastic peak (blue), which is also indicated by arrows.

## B. Inelastic Measurements And Shell-Model Calculations

Inelastic scattering measurements were carried out for in-the-scattering-plane geometry. Two typical TOF spectra showing diffusive elastic as well as inelastic peaks are shown in figure 5. The data were collected using beam

energies in the range of 25-65 meV. The high-energy He beam,  $E_i = 65$  meV, was used to probe the high-frequency surface phonon modes. The energy resolution for the lowest-energy beam was about 3 meV. Phonon energies and momenta were calculated from the TOF peak positions, after a Gaussian fit to the peaks, using Eqs. (1) and (2). To characterize the ensuing phonon dispersion points, lattice-dynamical analysis for the bulk and surface (slab calculation) was carried out.

### 1. Static equilibrium and bulk lattice dynamics

In lattice-dynamical studies of complex systems such as  $\text{LiCu}_2\text{O}_2$ , the construction of a dynamical matrix based on pair potentials rather than mere force constants is far more advantageous in the sense that the underlying physics is transparent and many of the potential parameters for similar pair interactions can be transferred from one compound to another. This is especially useful when experimental phonon frequencies are limited to a few bulk infrared (IR) and Raman active phonon modes at the center of the Brillouin zone (BZ)<sup>14,19</sup>, and no neutron-scattering data for phonon dispersion is available. Bulk lattice dynamics calculations, based on the shell-model, was used to obtain an empirical fit to existing IR and Raman data. The model incorporates

TABLE I: Best-fit Born-Meyer and shell parameters.

Born-Meyer Potential Parameters			
Bond	a(eV)	b( $\text{\AA}^{-1}$ )	c(eV $\text{\AA}^6$ )
Cu <sup>+1</sup> -O	18705.6	2.9	—
Cu <sup>+2</sup> -O	10000	4.4	—
Cu <sup>+1</sup> -Cu <sup>+2</sup>	3490.95	3.0	—
Cu <sup>+1</sup> -Cu <sup>+1</sup>	18853	3.0	—
Cu <sup>+2</sup> -Cu <sup>+2</sup>	6598.44	3.0	—
O — O	2146.30	3.4	50
Li — O <sup>a</sup>	840	3.0	—

shell model parameters			
Ion	Z(e)	Y(e)	K(eV/ $\text{\AA}^2$ )
Li	+1	1.5	5
Cu <sup>+1</sup>	+1	1.7	20
Cu <sup>+2</sup>	+2	2.9	30
O <sup>b</sup>	-2	-3.1	40

<sup>a</sup> ref.<sup>19</sup>, <sup>b</sup> ref.<sup>14</sup>

two-body central potentials, namely the Coulomb potential  $V_{ij}^C(r) = Z_i Z_j e^2 / r$  for the long-range interactions and either Born-Mayer  $V_{ij}(r) = a_{ij} e^{-b_{ij} r}$  or Buckingham  $V_{ij}(r) = a_{ij} \exp(-b_{ij} r) - c_{ij} / r^6$  potentials for the short-range interactions. The ionic shells are characterized by the ionic charge Z, the shell charge Y, and the intra-ion shell-core force constant K. Some of the initial short-range pair potentials were obtained from the literature: (Cu<sup>+2</sup>-O)<sup>14</sup>, (O-O)<sup>14</sup> and (Li-O)<sup>19</sup>. The remaining pair potential parameters were set to satisfy the static equilibrium conditions<sup>20</sup> which state that the forces on the particles in their equilibrium positions should vanish. This treatment also ensures the consistency of the static and dynamical properties of the crystal. It should

TABLE II: Comparison of experimental and calculated IR and Raman frequencies

Raman active			
Mode	Polarization	Frequency (cm <sup>-1</sup> )	
		Experiment <sup>9</sup>	Calculated
A <sub>g</sub>	aa	573	593.30
		497	—
		460	476.76
		367	375
		297	275.9
		178	191.33
		167	—
		122	108.86

IR active			
Mode	Polarization	Frequency (cm <sup>-1</sup> )	
		Experiment <sup>11</sup>	Calculated
B <sub>2u</sub>	b	240	—
		288	268.79
		312	—
		416	449.88
B <sub>3u</sub>	a	240	222.88
		288	269.621
		320	—
		392	375.54
		440	463.08/474.46

be noted, however, that satisfying static equilibrium conditions does not guarantee dynamical stability, namely ensuring the reality of the phonon frequencies throughout the BZ. It should also be noted that the shell-model parameters do not appear in the static equilibrium equations ions are treated as rigid bodies. However, these parameters are introduced into the dynamical matrix and are determined through the process of fitting the 17 ex-

perimental IR and Raman modes reported in the literature. The short-range potential and shell-model parameters that produce the best fit for these modes are listed in Table I. A comparison of the experimental and calculated values of these modes is given in Table II.

The complete set of calculated bulk phonon dispersion curves (60 branches) is shown in figure 6, along the high-symmetry directions  $\Gamma$ -X,  $\Gamma$ -Y and  $\Gamma$ -Z.

According to the point group  $mmm$  ( $D_{2h}$ ) of the space group  $Pnma$ , there are 30 Raman active and 27 IR active modes at the  $\Gamma$ -point, which are classified in terms of the corresponding irreducible representations as

$$10A_g \oplus 5B_{1g} \oplus 10B_{2g} \oplus 5B_{3g} \quad \text{Raman} \\ 9B_{1u} \oplus 4B_{2u} \oplus 9B_{3u} \quad \text{IR}$$

The remaining modes at the  $\Gamma$ -point include five  $A_u$  modes and 3 zero-frequency acoustic modes. The identification of the symmetries of the calculated modes at the  $\Gamma$ -point was established with the aid of the symmetry projection operators<sup>21</sup> of the point group  $mmm$ . Away from the  $\Gamma$ -point, the point group of the wave vector is isomorphic with  $C_{2v}$  for all 3 high-symmetry directions. Symmetry compatibility relations give

$C_{2v}$	$D_{2h}$		
	$\Delta(\langle 100 \rangle)$	$\Sigma(\langle 010 \rangle)$	$\Lambda(\langle 001 \rangle)$
$A_1$	$A_g$ $B_{3u}$	$A_g$ $B_{2u}$	$A_g$ $B_{1u}$
$A_2$	$A_u$ $B_{3g}$	$A_u$ $B_{2g}$	$A_u$ $B_{1g}$
$B_1$	$B_{1g}$ $B_{2u}$	$B_{1g}$ $B_{3u}$	$B_{3g}$ $B_{2u}$
$B_2$	$B_{2g}$ $B_{1u}$	$B_{3g}$ $B_{1u}$	$B_{2g}$ $B_{3u}$

In all, we have  $20A_1 \oplus 10A_2 \oplus 10B_1 \oplus 20B_2$  along the  $\langle 100 \rangle$ - and the  $\langle 001 \rangle$ -directions, and  $15A_1 \oplus 15A_2 \oplus 15B_1 \oplus 15B_2$  along the  $\langle 010 \rangle$ -direction.

The highest two bands ( $\simeq 800$ - $1200\text{cm}^{-1}$ ) are longitudinal optic phonons involving the motion of the eight  $\text{O}^{-2}$  ions in the primitive cell; in the upper band the four O1 ions at positions  $\{0.137, 1/4, 0.405\}$ ,  $\{0.363, 3/4, 0.905\}$ ,  $\{0.863, 3/4, 0.595\}$ ,  $\{0.637, 1/4, 0.095\}$  move in-phase with each other, but anti-phase with the four O2 ions at positions  $\{0.115, 1/4, 0.105\}$ ,  $\{0.385, 3/4, 0.605\}$ ,  $\{0.885, 3/4, 0.895\}$ ,  $\{0.615, 1/4, 0.395\}$ , while in the lower band, the O1 and O2 ions still have anti-phase motion, but also the ions at  $y = 1/4$  have anti-phase motion with those at  $y = 3/4$ . The lowest three bands (acoustic phonons)

mix with higher bands at higher  $\mathbf{q}$  vectors in the  $a$ - and  $b$ -directions, but remain distinct in the  $c$ -direction.

## 2. Lattice Dynamics of Slab-geometry and Surface Phonons

A lattice dynamics shell-model with slab-geometry consisting of 36 layers, and terminated with  $\text{Li}^{+1}\text{Cu}^{+2}\text{O}_2^{-2}$  surfaces, was used to calculate the phonon dispersion curves of that surface. Since translation symmetry is broken normal to the slab surfaces, primitive and non-primitive translations along this direction are not allowed. Consequently, the slab symmetry reduces to  $2ma$ , while the surface symmetry is  $p1m$ .

Surface equilibrium analysis showed that the  $\text{Cu}^{+2}$  and  $\text{Li}^{+1}$  surface ions have to be displaced outward, along the surface normal, from its bulk position, in order to satisfy equilibrium conditions in that direction. The pair potential and shell-model parameters of Table I were used in the initial slab calculations. However, the surface parameters had to be modified in order to achieve global stability in the entire surface BZ.

TABLE III: Character of the surface phonon dispersion curves. (Pol.:polarization, AP: anti-phase, IP: in-phase)

Branch	$\langle 10 \rangle$		$\langle 01 \rangle$		Type
	Ions	Pol.	Ions	Pol.	
$S_1$	$\text{Li}^{+1}$	$z$	$\text{Cu}^{+2}, \text{Li}^{+1}$ 1 : 5	$z$	AP ( $\langle 01 \rangle$ )
$S_2$	$\text{Cu}^{+2}$	$z$	$\text{Cu}^{+2}, \text{Li}^{+1}$ 5 : 1	$z$	IP ( $\langle 01 \rangle$ )
$S_3$	$\text{Cu}^{+2}$	$y$	$\text{Cu}^{+2}$	$x$	
$S_4$	$\text{Cu}^{+2}$	$x$	$\text{Cu}^{+2}$	$y$	
$S_5$	$\text{O}^{-2}$	$z$	$\text{O}^{-2}$	$z$	
$S_6$	$\text{Li}^{+1}$	$y$	$\text{Li}^{+1}$	$x$	
$S_7$	$\text{Li}^{+1}$	$x$	$\text{Li}^{+1}$	$y$	
$S_8$	$\text{O}^{-2}$	$y$	$\text{O}^{-2}$	$x$	IP
$S_9$	$\text{O}^{-2}$	$y$	$\text{O}^{-2}$	$y$	AP
$S_{10}$	$\text{O}^{-2}$	$x$	$\text{O}^{-2}$	$x$	AP

The resulting surface phonon dispersion curves are shown as blue dots superimposed on a gray background in figure 7; they are labeled  $S_i$ ,  $i = 1, \dots, 10$ . The gray background areas and lines resulting from the slab calculations correspond to contributions from the slab bulk, namely projections onto the surface BZ. Some of the dispersed gray lines would turn into solid bands as the thickness of the slab approaches infinity. The general character of the surface modes  $S_1 - S_{10}$  is given in Table III.  $S_1$  and  $S_2$  involve the motions of the  $\text{Cu}^{+2}$  and  $\text{Li}^{+1}$  normal

to the surface. While  $S_1$  is quite flat for wave vectors  $q \simeq 0.15 - 0.5(2\pi/a)$  along the  $a$ -direction, it exhibits anomalous softening in the proximity of the surface BZ boundary along the  $b$ -direction. This softening could be the result of the tenuous equilibrium of these ions normal to the surface.

The scattering of He beams with energies in the range 25-65 meV allows measurement of surface phonons with frequencies below  $400 \text{ cm}^{-1}$  (50 meV). Thus we will focus on identifying the measured inelastic scattering events with calculated surface phonon dispersion curves in that range. The process of identification is further complicated by the presence of twinning in the sample crystals. A successful procedure must be capable of sorting out modes propagating in the  $a$ -direction from those propagating in the  $b$ -direction. Figure 8(a) illustrates this complexity. Here, all measured inelastic events are plotted in the left and right panels, after reducing their momenta to the first surface BZ along the  $a$ -direction (left panel) and along the  $b$ -direction (right panel). Notice that each measured inelastic event has a different value of its reduced momentum for the different directions. The sorting criterion adopted, was to assign a given event to the direction where it is nearest in energy to a disper-

sion curve. The final result is plotted in figure 8(b). The agreement is surprisingly quite good, especially with the two low-lying dispersion curves. In addition, this agreement supports the surface termination analyzed in this paper.

In summary, with the aid of He scattering techniques at room temperature, we find that the (001) surface of  $\text{LiCu}_2\text{O}_2$  is exclusively terminated by  $\text{Li}^{+1}\text{Cu}^{+2}\text{O}_2^{-2}$ , and that no surface reconstruction occurs. Empirical fitting of lattice dynamics shell-model based calculations to measured inelastic He scattering spectra, supports the proposed termination and reveals that the lowest surface phonon dispersion branches involve the motion of  $\text{Cu}^{+2}$  and  $\text{Li}^{+1}$  ions normal to the surface.

### Acknowledgement

This work is supported by the U.S. Department of Energy under Grant No. DE-FG02-85ER45222. FCC acknowledges the support from National Science Council of Taiwan under project number NSC-95-2112-M-002.

- 
- <sup>1</sup> T. Masuda, A. Zheludev, A. Bush, M. Markina, and A. Vasiliev, Phys. Rev. Lett. **92**, 177201 (2004).
  - <sup>2</sup> T. Masuda, A. Zheludev, B. Roessli, A. Bush, M. Markina, and A. Vasiliev, Phys. Rev. B **72**, 014405 (2005).
  - <sup>3</sup> L. Mihály, B. Dóra, A. Ványolos, H. Berger, and L. Forró, Phys. Rev. Lett. **97**, 067206 (2006).
  - <sup>4</sup> H. J. Xiang and M.-H. Whangbo, Phys. Rev. Lett. **99**, 257203 (2007).
  - <sup>5</sup> S. W. Huang, D. J. Huang, J. Okamoto, C. Y. Mou, W. B. Wu, K. W. Yeh, C. L. Chen, M. K. Wu, H. C. Hsu, F. C. Chou, et al., Phys. Rev. Lett. **101**, 077205 (2008).
  - <sup>6</sup> S. Seki, Y. Yamasaki, M. Soda, M. Matsuura, K. Hirota, and Y. Tokura, Phys. Rev. Lett. **100**, 127201 (2008).
  - <sup>7</sup> S. Park, Y. J. Choi, C. L. Zhang, and S.-W. Cheong, Phys. Rev. Lett. **98**, 057601 (2007).
  - <sup>8</sup> A. A. Gippius, E. N. Morozova, A. S. Moskvina, A. V. Zalessky, A. A. Bush, M. Baenitz, H. Rosner, and S.-L. Drechsler, Phys. Rev. B **70**, 020406 (2004).
  - <sup>9</sup> K.-Y. Choi, Zvyagin, S. A., Cao, G., and P. Lemmens, Phys. Rev. B **69**, 104421 (2004).
  - <sup>10</sup> S. Zvyagin, G. Cao, Y. Xin, S. McCall, T. Caldwell, W. Moulton, L.-C. Brunel, A. Angerhofer, and J. E. Crow, Phys. Rev. B **66**, 064424 (2002).
  - <sup>11</sup> M. Papagno, D. Pacilé, G. Caimi, H. Berger, L. Degiorgi, and M. Grioni, Phys. Rev. B **73**, 115120 (2006).
  - <sup>12</sup> R. Berger, J. Alloys and Compounds **184**, 315 (1992).
  - <sup>13</sup> H. C. Hsu, H. L. Liu, and F. C. Chou, Phys. Rev. B **78**, 212401 (2008).
  - <sup>14</sup> M. Farzaneh, X.-F. Liu, M. El-Batanouny, and F. C. Chou, Phys. Rev. B **72**, 085409 (2005).
  - <sup>15</sup> K. Martini, W. Franzen, and M. El-Batanouny, Rev. Sci. Instrum. **58**, 1027 (1987).
  - <sup>16</sup> D. Farias and K.-H. Rieder, Rep. Prog. Phys. **61**, 1575 (1998).
  - <sup>17</sup> U. Garibaldi, A. Levi, R. Spadacini, and G. Tommei, Surface Science **48**, 649 (1975).
  - <sup>18</sup> K. Rieder, N. Garcia, and V. Celli, Surface Science **108**, 169 (1981).
  - <sup>19</sup> R. A. Jackson and M. E. Valerio, J. Phys.: Condensed Matter **17**, 837 (2005).
  - <sup>20</sup> D. A. Zatsepin, V. R. Galakhov, M. A. Korotin, V. V. Fedorenko, E. Z. Kurmaev, S. Bartkowski, M. Neumann, and R. Berger, Phys. Rev. B **57**, 4377 (1998).
  - <sup>21</sup> M. El-Batanouny and F. Wooten, *Symmetry and Condensed Matter Physics: A Computational Approach* (Cambridge University Press, 2008).



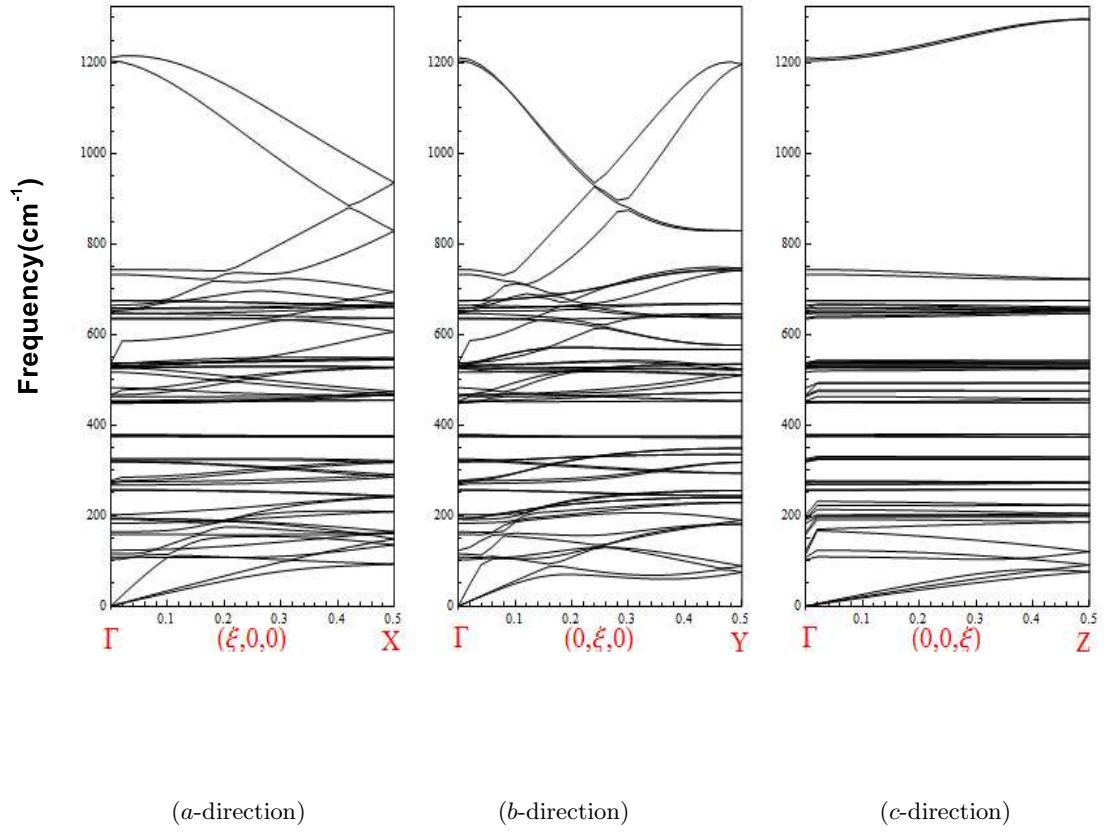


FIG. 6: Bulk phonon dispersion curves along **a** ( $\xi = q/G_a$ ), **b** ( $\xi = q/G_b$ ) and **c** ( $\xi = q/G_c$ ).



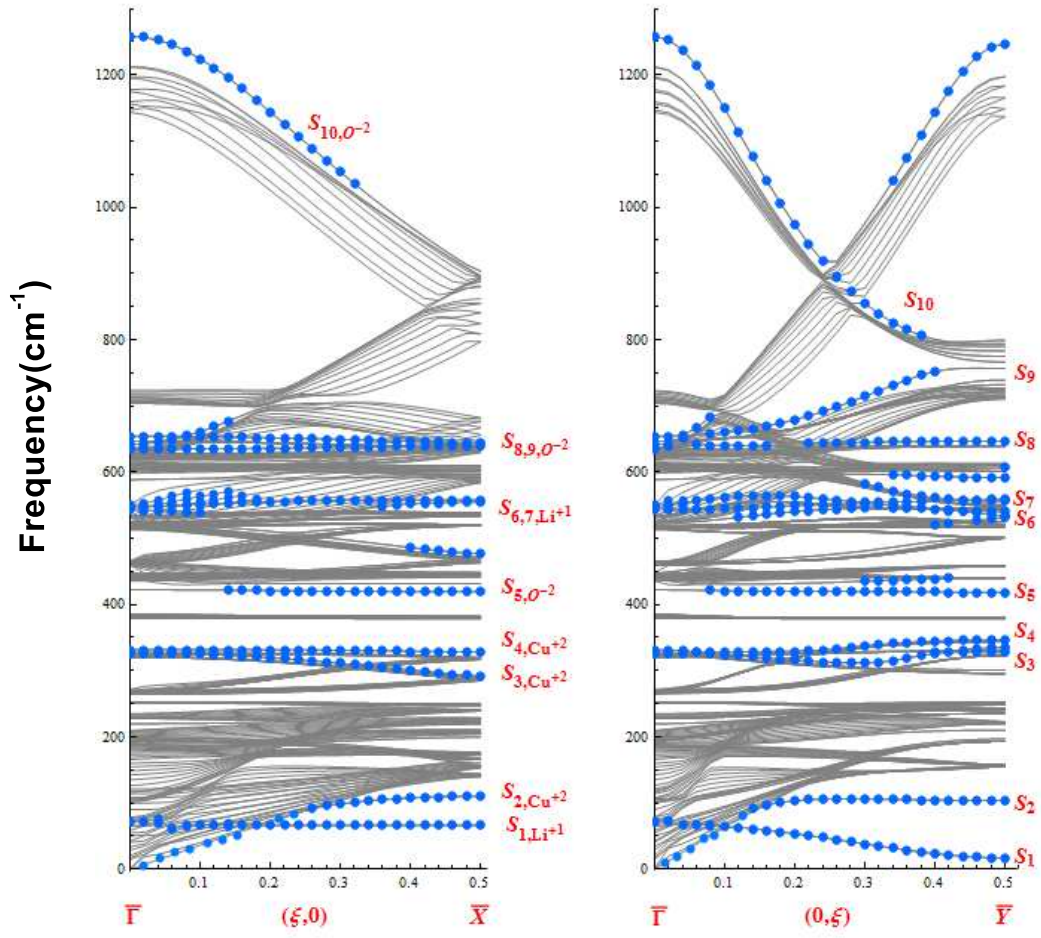


FIG. 7: Surface phonon dispersion curves, indicated by blue dots superimposed on a gray background. The latter represents the surface projection of bulk bands on the surface BZ. The surface modes are labeled  $S_i$ ,  $i = 1, \dots, 10$ .

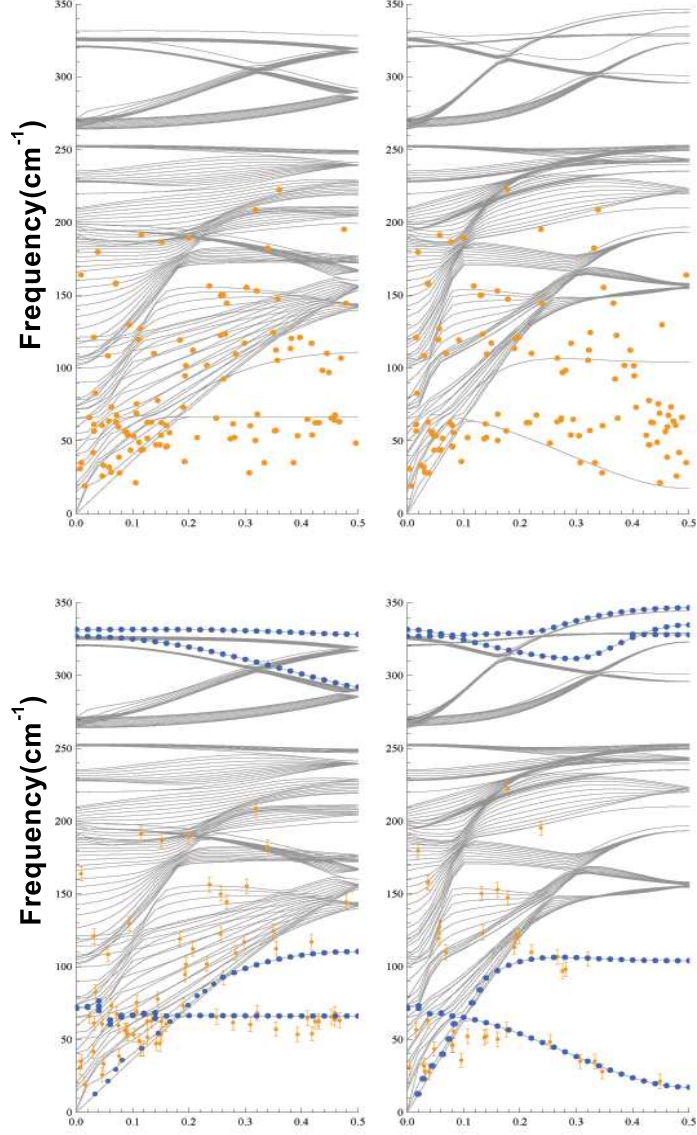


FIG. 8: Top panels: All measured inelastic events, reduced to the proper surface BZ, superposed on calculated dispersion curves along  $\langle 10 \rangle$ , (left panel), and  $\langle 01 \rangle$  (right panel). Lower panels: Fits obtained by the procedure described in the main text for  $\langle 10 \rangle$ , (left panel), and  $\langle 01 \rangle$  (right panel). (Error bars are also indicated in the lower panels).